ACS APPLIED ENERGY MATERIALS

www.acsaem.org Article

Dual-Size TiO_2 Nanoparticle-Engineered Interfaces for Broadband Light Scattering and Efficiency Enhancement in Perovskite Solar Cells

Raji Radhakrishnan, Jung Keun Cha, and Soo Hyung Kim*

Cite This: *ACS Appl. Energy Mater.* 2025, 8, 14893−14901 Read Online

ACCESS | Metrics & More | Article Recommendations

Downloaded via PUSAN NATL UNIV on October 14, 2025 at 09:44:28 (UTC).
See https://pubs.acs.org/sharingguidelines for options on how to legitimately share published articles.

ABSTRACT: While power conversion efficiencies (PCEs) of perovskite solar cells (PSCs) can be improved by incorporating sophisticated nanostructures into the electron transport layer (ETL), conventional approaches in this regard are often limited by complex fabrication processes and poor reproducibility. In this study, we propose a simple and efficient strategy involving a mixed ETL composed of two types of TiO_2 nanoparticles (NPs) with different average sizes (15 and 250 nm) to improve the photovoltaic performance of PSCs. The 15 nm TiO_2 NPs primarily function as efficient electron transporters, facilitating the extraction and transfer of photogenerated electrons from the perovskite layer. The larger 250 nm TiO_2 NPs serve as effective light-scattering centers that enhance light-harvesting efficiency by increasing the optical path length within the active layer. The scattering effects are examined using the principles of Rayleigh and Mie scattering theories. The 250 nm TiO_2 NPs, with particle sizes comparable to or larger than the incident light wavelength, follow Mie scattering, leading to significant forward and backward scattering that enhances light trapping in the active layer. Conversely, the 15 nm TiO_2 NPs, being considerably smaller than the incident wavelength, predominantly follow Rayleigh scattering, as characterized by wavelength-dependent scattering intensity, thus contributing minimally to light redirection while ensuring high electron conductivity. Overall, we achieve a synergistic effect between enhanced light scattering and efficient charge transport by optimizing the ratio of the TiO_2 NPs, thereby improving the overall PCE of PSCs.

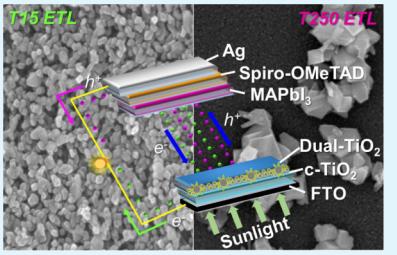

KEYWORDS: *TiO_2 nanoparticle, light scattering, perovskite solar cells, Rayleigh−Mie synergy, efficiency improvement*

1. INTRODUCTION

The ongoing energy crisis and the increasing recognition of the necessity for sustainable energy have accelerated the development of renewable energy technologies. Among them, solar energy is considered a promising source of renewable energy. Organic−inorganic solar cells, a type of photovoltaic device, offer several advantages such as flexibility, lightweight, low cost, and applicability to large-area flexible substrates.[1] Recent progress in the development of organic−inorganic solar cells has been driven by the continuing emergence of novel materials and device fabrication technologies.[2] Among the various types of organic−inorganic solar cells, perovskite solar cells (PSCs) have attracted significant attention, considering their power conversion efficiency (PCE) has improved dramatically from approximately 3.8% in the initial years to approximately 25.5% currently.[3,4] The excellent optoelectronic properties of perovskites—such as facile crystal growth as a cubic structure, broad absorption range well-matched with the solar spectrum, low exciton binding energy, and long carrier diffusion length—highlight their strong potential as energy-harvesting materials.[5−8] However, despite their remarkable potential, their large-scale production and commercialization remain hindered owing to numerous technical challenges.

In a typical PSC, the active perovskite layer composed of CH_3PbX_3 (X = Cl^-, Br^-, I^-) is sandwiched between an electron transport layer (ETL) and a hole transport layer (HTL), which are in contact with metal electrodes.[9] Excitons are generated when sunlight is incident on the active layer, and the resulting electrons and holes are collected at the respective electrodes. Therefore, efficient extraction of charge carriers and effective utilization of sunlight are critical factors in enhancing the device performance of PSCs. Various approaches, including materials engineering, device architecture optimization, light management, and improvement of thin-film quality, have been explored to address these challenges.[10−12] A range of HTL materials has been developed to date, including NiO_x,[13] CuSCN,[14] PEDOT:PSS (poly(3,4-ethylenedioxythiophene) polystyrenesulfonate),[15] PTAA (poly(triarylamine)),[16] and Spiro-OMeTAD (2,2“,7,7”-tetrakis(N,N-di-*p*-methoxyphenyl-

Received: August 21, 2025
Revised: September 8, 2025
Accepted: September 10, 2025
Published: September 15, 2025

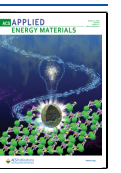

ACS Publications © 2025 American Chemical Society

amine)-9,9'-spirobifluorene).[17] Among them, Spiro-OMeTAD is the most widely used HTL material and exhibits excellent PCE when used in conjunction with metal electrodes such as Au, Ag, or Al.[18−21] The ETL plays a key role in extracting the photogenerated electrons from the perovskite layer. However, improving the quality of the ETL remains a significant challenge in further enhancing the overall performance and PCE of PSCs. Semiconductor materials, such as TiO_2,[22,23] ZnO,[24] SnO_2,[6,6,25] -phenyl-C_{61}-butyric acid methyl ester (PCBM),[26] and CdS,[27,28] have been employed as ETL materials in PSCs. Among them, TiO_2 is the most used photocatalyst-based ETL material, and various nanostructured forms, including nanowires, nanodendrites (NDs), nanoparticles (NPs), and well-aligned mesoporous structures of TiO_2, have been considered. In particular, mesoporous TiO_2 (m-TiO_2) has attracted greater attention than planar structures owing to its large surface area, high porosity, and increased interfacial contact area, which facilitate the infiltration of the perovskite precursor solution, enhance the extraction of photogenerated electrons, and reduce hysteresis.[29−33] While introducing mesoporous ETL scaffolds and efficient HTLs contributes significantly to improving the PCE of PSCs, the enhancement of light absorption in the perovskite absorber layer also plays a crucial role. An increase in light absorption leads to an increase in the number of generated electron−hole pairs, which results in a higher current density and, ultimately, better device performance.

Yang et al.[34] introduced TiO_2 NPs/nanotubes (NTs) into the active layer of PSCs. Consequently, the short-circuit current density (J_{sc}) increased significantly from 23.9 mA/cm^2 (without NTs) to 25.5 mA/cm.^{2} The TiO_2 NTs improved light harvesting efficiency and charge conduction. Lin et al.[35] developed a methylammonium lead iodide ($MAPbI_3$) solar cell based on TiO_2 NDs. $MAPbI_3$ was incorporated into the interstices of a quasi-single-crystalline TiO_2 ND array. The resulting matrix exhibited superior light trapping, higher photoelectron extraction, and higher internal quantum efficiency. Compared to a $MAPbI_3$−TiO_2 nanorod-based device, this cell exhibited a 22% and 25% increase in the average J_{sc} and PCE, respectively. Kim et al.[36] applied a facile nanoimprinted one-dimensional grating nanopattern (1D GNP) onto m-TiO_2 to develop a cesium-based all-inorganic halide perovskite (CsPe) device. The 1D GNP on the ETL diffracted unabsorbed light back into the m-TiO_2 and $CsPbIBr_2$ layers, significantly enhancing light absorption efficiency. In addition, the enlarged interfacial contact area facilitated effective charge separation and collection. Consequently, the J_{sc} and fill factor (FF) of the fabricated solar cell increased, ultimately leading to a > 20% increase in the PCE. Li et al.[37] employed a bilayer TiO_2/SnO_2 ETL in PSCs. This bilayer structure improved charge extraction and reduced carrier recombination at the ETL/perovskite interface, thereby enhancing the separation and transport of photogenerated carriers. The fabricated PSC achieved a PCE of 19.11% and a J_{sc} of 22.77 mA/cm.^{2} In comparison, devices using a single ETL composed of either SnO_2 or TiO_2 exhibited lower performance, with PCEs of 17.40 and 14.76%, respectively, and J_{sc} values of 21.63 and 19.92 mA/cm,^{2} respectively.

While incorporating sophisticated nanostructures into the ETL to improve the PCE of PSCs has been extensively investigated, such approaches often involve complex fabrication processes and are limited by poor reproducibility. In this study, we propose a simpler and more efficient strategy by applying a mixed ETL composed of two types of TiO_2 NPs with different average sizes (15 and 250 nm). The light scattering behavior within the ETL can be effectively tailored by controlling the NP size to extend the path length of the incident light and enhance light absorption efficiency. The 15 nm TiO_2 NPs, being considerably smaller than the wavelength of visible light, induce Rayleigh scattering, resulting in a uniform light distribution across the active layer and enhanced uniform light absorption. The 250 nm TiO_2 NPs, with dimensions comparable to visible wavelengths, generate Mie scattering, which strongly redirects incident light along specific directions, thus enabling light retention within the active layer for an extended duration and, consequently, maximizing light absorption. This dual-particle blending approach enables the simultaneous induction of both Rayleigh and Mie scattering, facilitating the formation of an effective light-trapping structure within the ETL without requiring complicated nanostructuring processes. This approach is expected to contribute significantly to improving the performance of PSCs. In this work, we fabricated PSCs using a low-cost and facile spin-coating method, incorporating mixed ETL films based on TiO_2 NPs of different sizes. The correlation between light scattering characteristics and the resulting photovoltaic performance was systematically investigated by varying the mixing ratio of T_{15} (TiO_2 NPs with an average size of 15 nm, enhancing photon absorption) and T_{250} (TiO_2 NPs with an average size of 250 nm, promoting photon scattering).

2. EXPERIMENTAL METHODS

2.1. Materials. Fluorine-doped tin oxide (FTO) glass substrates were purchased from Pilkington Tech (Boston, MA) and were used as the transparent electrode substrates for PSCs in this study. Titanium dioxide NP pastes—T/SP (T_{15}) and WER2-O (T_{250})—used for the ETL in the photoactive layer of the PSCs were purchased from Solaronix (Switzerland) and Greatcell Solar (Australia), respectively. Various solutions and chemicals used for the formation of the crystalline and porous structures of the perovskite during the fabrication of the photoactive layer of the PSCs, including acetone, ethanol, acetic acid (≥99.7%), terpineol, diisopropoxide bis-(acetylacetonate) (75 wt % in isopropanol), 4-*tert*-butylpyridine (96%), and dimethylformamide (DMF), were purchased from Sigma-Aldrich. The following materials were used for the formation of the HTL of the PSCs: 1-butanol (Junsei Chemical Co., Ltd.), dimethyl sulfoxide (DMSO; 99.8%; Alfa Aesar), chlorobenzene (CB; anhydrous; 99.8%), lead iodide (PbI_2; 99.99%; Tokyo Chemical Industry Co., Ltd.), methylammonium iodide (CH_3NH_3I; Sigma-Aldrich), diethyl ether (≥99.7%; Sigma-Aldrich), lithium bis-(trifluoromethanesulfonyl)imide (Li-TFSI; Sigma-Aldrich), and Spiro-OMeTAD (Sigma-Aldrich). Silver (Ag; 99.99%) used for the PSC electrodes was purchased from Taewon Scientific Co., Ltd. (South Korea).

2.2. Device Architecture. $CH_3NH_3PbI_3$-based PSCs were fabricated with an ETL using various mixing ratios of T_{15} and T_{250} (T_{15}:T_{250} = 10:0, 7:3, 5:5, 3:7, and 0:10). All precursor solutions were coated onto the FTO glass inside a dehumidifying glovebox.

2.2.1. FTO Precleaning. A substrate composed of FTO (SnO_2:F) with dimensions of 25 × 25 mm, thickness of 0.2 mm, and FTO sheet resistance of 15 Ω/sq was used as the transparent electrode material. The FTO glass was precleaned using an ultrasonic cleaner (power: 665 W, frequency: 60 kHz)

https://doi.org/10.1021/acsaem.5c02634
ACS Appl. Energy Mater. 2025, 8, 14893−14901

in acetone, ethanol, and deionized water for 15 min each. Thereafter, the FTO glass substrates were dried using a nitrogen (N_2) gun.

2.2.2. TiO_2-Based ETL Deposition (Step 1). We prepared a TiO_2-based ETL solution by mixing T_{15} and T_{250} in various ratios. The precleaned FTO glass substrates were placed in a Petri dish and heat-treated with 20 mL of $TiOCl_2$ solution (prepared by diluting 0.247 mL of $TiOCl_2$ in 20 mL of deionized water) at 70 °C for 30 min to improve the adhesion of the TiO_2 NPs in the mixed ETL solution to the surface of the FTO glass substrate. After heat treatment, the FTO glass substrates were rinsed with deionized water and annealed in a box furnace at 500 °C for 30 min. Before depositing the mixed ETL solution, a compact TiO_2 (c-TiO_2) layer—composed of titanium diisopropoxide bis(acetylacetonate) (75 wt % in isopropanol) dissolved in 1-butanol—was deposited on the pretreated FTO glass via spin-coating. The spin-coating was conducted at 700 rpm for 8 s, 1000 rpm for 10 s, and 2000 rpm for 40 s, followed by drying at 125 °C for 5 min. Subsequently, a mixed ETL solution with various compositions (where S1, S2, S3, S4, and S5 represent mixing ratios of T_{15}:T_{250} = 10:0, 7:3, 5:5, 3:7, and 0:10, respectively; see Table 1) was prepared for spin-coating the TiO_2 thin films. The solution comprised anhydrous ethanol (5 mL), a 1:1 mixture of acetic acid (50 μL) and α-terpineol (50 μL), and 0.125 g of ethyl cellulose as a polymer template. This solution was coated onto the c-TiO_2-coated FTO glass and dried at 100 °C for 5 min. Finally, the ETL-coated FTO glass substrates were annealed at 550 °C for 1 h.

Table 1. Various Mixing Ratios of T_{15} and T_{250} Used in ETL of the PSCs

Sample	Mixing ratio (T_{15}:T_{250})	T_{15} (g)	T_{250} (g)
S1	10:0	0.30	0.00
S2	7:3	0.21	0.09
S3	5:5	0.15	0.15
S4	3:7	0.09	0.21
S5	0:10	0.00	0.30

2.2.3. $MAPbI_3$-Based Perovskite Layer (PL) Deposition (Step 2). The perovskite precursor solution was prepared by mixing PbI_2 (461 mg) and CH_3NH_3I (159 mg) in 71 μL DMSO and 520 μL DMF. The solution was heated at 70 °C under constant stirring for 1 h and then filtered using a polytetrafluoroethylene (PTFE) filter (pore size: 0.20 μm, filter diameter: 13 mm). A suitable amount of the precursor solution (~32 μL) was spin-coated onto the ETL-coated FTO glass substrate at 4000 rpm for 25 s. After 5 s of spinning, 0.5 mL of diethyl ether (antisolvent) was slowly dropped onto the rotating substrate. Adding the antisolvent facilitates rapid nucleation and smooth, uniform growth of the perovskite crystallites. After spin coating, the substrate was heated at 70 °C for 2 min and then further heated at 100 °C for 7 min, resulting in a deep brown, highly dense, shiny, and uniform PL.

2.2.4. Spiro-OMeTAD-Based HTL Deposition (Step 3). The Spiro-OMeTAD precursor solution, used as the hole transport material, was prepared by dissolving 2,2′,7,7′-tetrakis (N, N′-di-*p*-methoxyphenyl amine)-9,9′-spirofluorene (72.3 mg) in 1 mL of CB. A clear pale-yellow solution was obtained; subsequently, 4-*tert*-butylpyridine (28.8 μL) and 17.5 μL of Li-TFSI (P-dopant) stock solution (520 mg dissolved in 1 mL acetonitrile) was added to it. The prepared solution was heated at 70 °C under constant stirring for 1 h and then filtered using a PTFE filter. Next, 32 μL of the Spiro-OMeTAD precursor solution was spin-coated onto the PL at 3000 rpm for 30 s. The HTL-coated sample was placed in a drybox overnight under dark conditions to facilitate the oxidation of Spiro-OMeTAD.

2.2.5. Thermal Evaporation of Ag-Based Back Contact (Step 4). The back contact, composed of silver (Ag) with a thickness of approximately 100 nm, was thermally evaporated (pressure: 1.6×10^{-5} Torr, deposition rate: ~ 1.0−1.5 Å/s) over the HTL layer. A schematic of the experimental fabrication of each layer of the PSCs is presented in Figure 1.

2.2.6. PCE and IPCE Measurement of PSCs (Step 5). The photovoltaic performance of the fabricated solar cell was measured under standard AM 1.5 G (air mass 1.5 Global) conditions and stimulated light intensity of ~1000 W/m.[2] The PCE was measured using a solar simulator (PEC-L11, Peccell

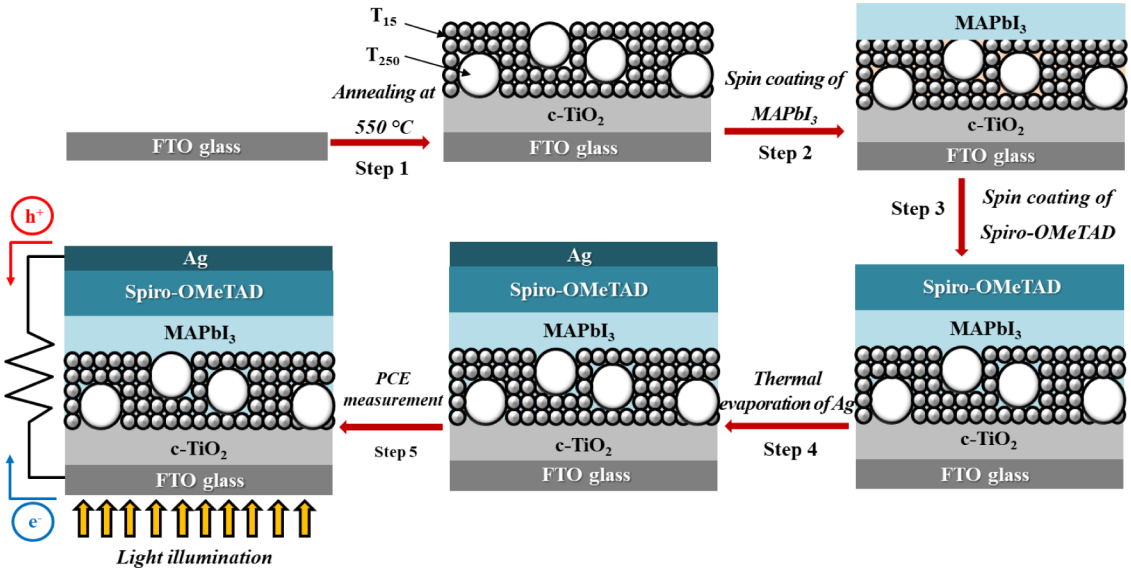

Figure 1. Schematic illustration of the experimental fabrication procedure for PSCs.

https://doi.org/10.1021/acsaem.5c02634
ACS Appl. Energy Mater. 2025, 8, 14893−14901

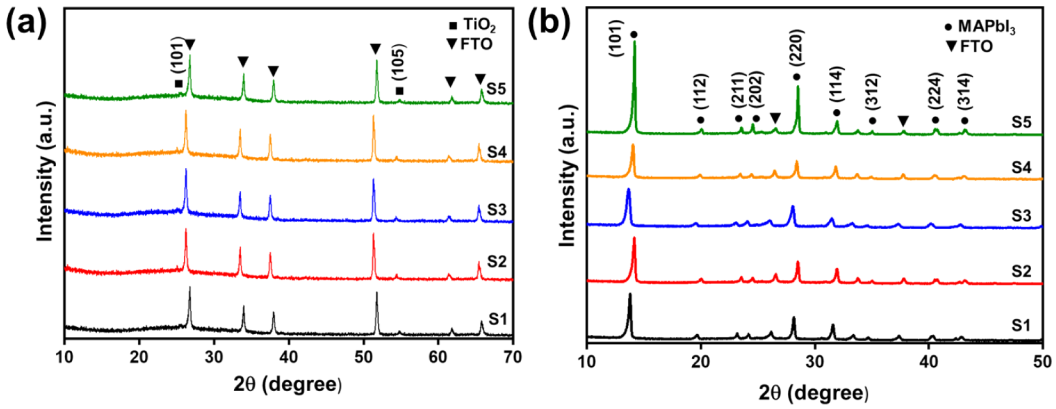

Figure 2. XRD patterns of (a) electron transport layer (ETL) thin films (TFs) and (b) $MAPbI_3$ perovskite layers (PLs)-coated ETL TFs composed of T_{15} and T_{250} mixtures with various mixing ratios: S1 (T_{15}:T_{250} = 10:0), S2 (7:3), S3 (5:5), S4 (3:7), and S5 (0:10).

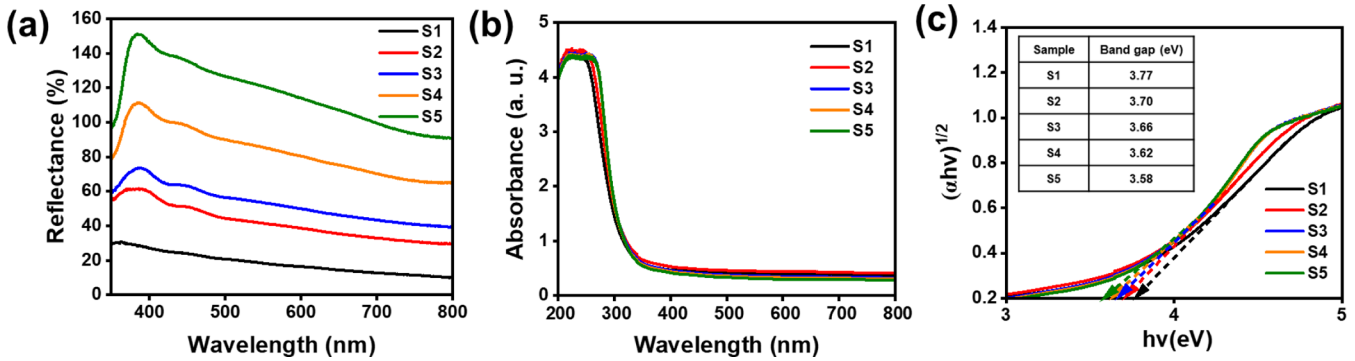

Figure 3. UV−vis spectra of FTO glass substrates coated with electron transport layer (ETL) thin films (TFs) incorporating different T_{15}:T_{250} mixing ratios: (a) diffuse reflectance, (b) absorbance, and (c) Tauc plots for samples S1−S5. The samples correspond to the following compositions: S1 (T_{15}:T_{250} = 10:0), S2 (7:3), S3 (5:5), S4 (3:7), and S5 (0:10).

Technologies, Inc., Japan) calibrated with a Si solar cell. A shadow mask with an active area of 0.06 cm^2 was used during the measurements. For each composition, five PSCs were fabricated under identical conditions, and the average performance values along with standard deviations for short circuit current (J_{sc}), open circuit voltage (V_{oc}), fill factor (FF), and PCE were determined to ensure statistical reliability. In addition, the incident photon-to-electron conversion efficiency (IPCE) spectra were obtained in the 300−900 nm range using another solar simulator (PEC-S20, Peccell Technologies, Inc., Kanagawa, Japan).

2.3. Material and Device Characterization. The crystalline properties of the ETL thin film (TF) within the photoactive layer of PSCs were investigated via X-ray diffraction (XRD) analysis (Miniflex II, Rigaku, Japan) using 1.542 Å Cu Kα radiation in a Bragg−Brentano configuration. The surface morphology of the TiO_2 NP-based ETL TF was examined via field emission scanning electron microscopy (FE-SEM; S4700, Hitachi, Japan). The cross-sectional structure of the ETL was observed via high-resolution low-voltage scanning electron microscopy (HRLV-SEM; JSM-7900F, Jeol, Japan). A thin platinum layer (approximately 8−10 nm) was coated on the surface of the ETL sample to enhance conductivity before the FE-SEM and HRLV-SEM measurements. The optical absorbance properties of the TiO_2-based ETL were measured using an ultraviolet−visible (UV−Vis) and near-infrared (NIR) spectrometer (V770, Jasco, Japan), and the diffuse reflectance spectra of light were measured over a 200−800 nm wavelength range using another UV−Vis and NIR spectrometer (Carry 5000, Agilent, USA).

3. RESULTS AND DISCUSSION

Figure 2a shows the XRD patterns of ETL TFs with various mixing ratios of T_{15} and T_{250} (i.e., cases S1−S5). The FTO glass substrates coated with ETL TFs were irradiated within the 2θ range of 10−70°, with a scan step size of 0.013°. The XRD peaks were in excellent agreement with JCPDS card no. 21−1272 (anatase-phase TiO_2). The distinct diffraction peaks observed at the (101) and (105) planes of the anatase crystal structure confirmed its high crystallinity and purity. Other peaks corresponded to the FTO substrate, and no additional impurity peaks were observed. Figure 2b presents the XRD pattern of $MAPbI_3$-based PLs formed on the FTO/c-TiO_2/m-TiO_2 substrate in the 2θ range of 10−50°. The peaks at 14.1°, 20.0°, 23.5°, 24.5°, 28.5°, 31.9°, 33.9°, 40.7°, and 43.2° corresponded to the crystal planes (110), (112), (211), (202), (220), (114), (312), (224), and (314), respectively, of the $MAPbI_3$ perovskite.[38] The absence of the PbI_2 peak at approximately 12.6° in all sample patterns indicated the complete conversion of PbI_2 into $MAPbI_3$. This result further confirmed the formation of pure $MAPbI_3$ PLs.

The light scattering effects of T_{15} and T_{250} were investigated by measuring the diffuse reflectance and reflection spectra of the five samples (S1−S5) with various mixed ETL TFs of T_{15} and T_{250} in the wavelength range of 300−800 nm, and the results are shown in Figure 3. The results of the optical spectrum analysis, shown in Figure 3a, indicate that the diffuse

https://doi.org/10.1021/acsaem.5c02634
ACS Appl. Energy Mater. 2025, 8, 14893−14901

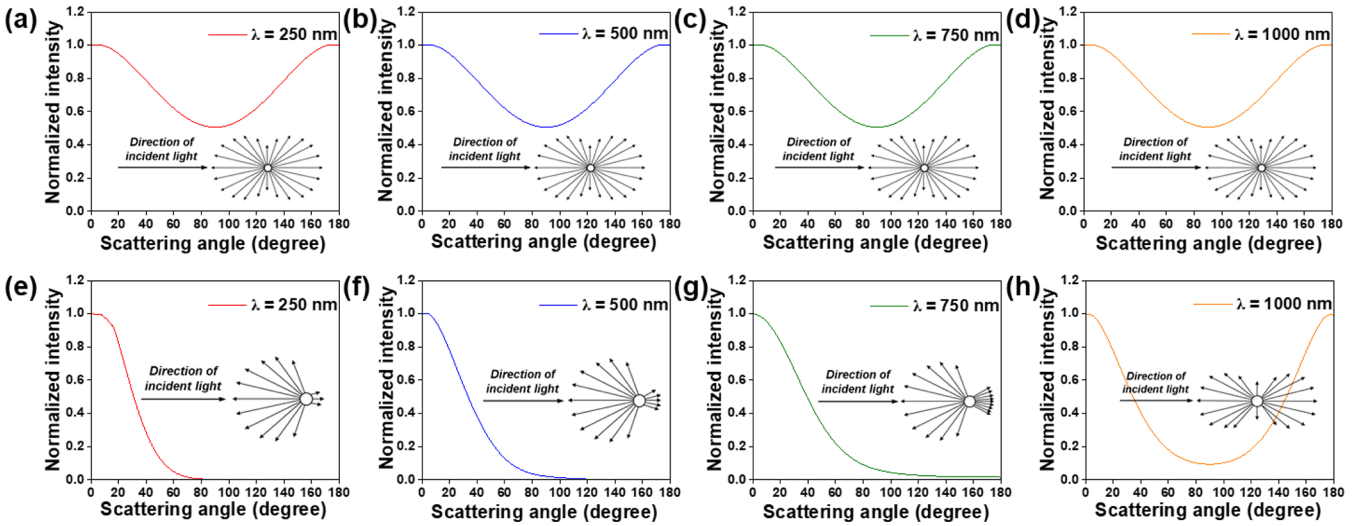

Figure 4. Normalized angular scattering intensity distributions for T_{15} nanoparticles (NPs) under incident light at four different wavelengths of (a) λ = 250, (b) 500, (c) 750, (d) 1000 nm and for T_{250} NPs under incident light at four different wavelengths of (e) λ = 250, (f) 500, (g) 750, (h) 1000 nm.

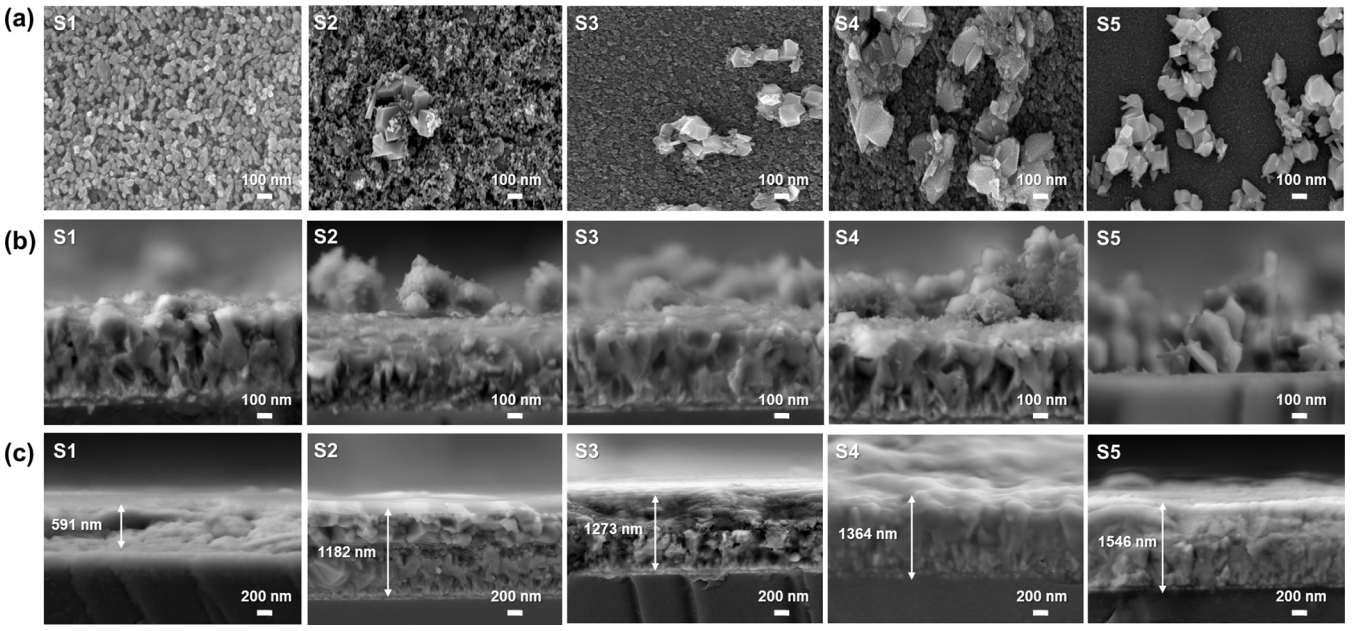

Figure 5. FE-SEM images of electron transport layer (ETL) thin films (TFs) incorporating different T_{15}:T_{250} mixing ratios: (a) top-view images and (b) cross-sectional images of TFs for each sample—S1 (T_{15}:T_{250} = 10:0), S2 (7:3), S3 (5:5), S4 (3:7), and S5 (0:10). (c) HRLV-SEM cross-sectional images of full device structures (FTO/c-TiO_2/m-TiO_2/$MAPbI_3$/Spiro-OMeTAD) fabricated with the same T_{15}:T_{250} mixing ratios.

reflectance of the ETL TFs increased across all wavelength ranges with an increase in the T_{250} content. Among the ETL TF samples, S5 (T_{15}:T_{250} = 0:10) exhibited the highest reflectance, attributed to the strong forward scattering effect induced by the large T_{250} NPs. In contrast, S1, composed of T_{15} NPs alone (and no large T_{250} NPs), exhibited the lowest reflectance. In all samples, the reflectance intensity decreased gradually at wavelengths greater than 450 nm. Considering a lower optical reflectance implies higher light absorption, this phenomenon is considered a crucial factor for enhancing the ETL performance in optoelectronic devices. Figure 3b presents the UV−Vis absorbance spectra of various mixed ETL TFs of T_{15} and T_{250}. Notably, S2 (T_{15}:T_{250} = 7:3) exhibited the highest light absorption, explained as follows: T_{250} NPs is distributed within the T_{15} NP matrix act as a highly effective light-scattering medium, generating multiple light-scattering pathways and thereby significantly increasing the light propagation distance within the ETL TFs. In contrast, S5, which exhibited the lowest absorbance, contained only T_{250} NPs in the ETL TFs. Consequently, the light scattering effect was maximized, while the light absorption capability was significantly reduced. The Tauc plot (Figure 3c) illustrates the bandgap variation across samples S1−S5 with different TiO_2 nanoparticle sizes. A clear decreasing trend in bandgap energy (from 3.77 eV for S1 to 3.58 eV for S5) is observed, indicating that smaller particles exhibit wider bandgaps due to quantum confinement effects, while larger particles result in narrower gaps. Mixed samples (S2−S4) show intermediate values, suggesting that dual-particle integration modifies the electronic environment beyond light scattering. These results imply that

https://doi.org/10.1021/acsaem.5c02634
ACS Appl. Energy Mater. 2025, 8, 14893−14901

particle size variation affects both optical and electronic properties of the ETL.

The light scattering characteristics of T_{15} and T_{250} NPs were investigated by visualizing the angular scattering intensity profiles at different incident light wavelengths (λ = 250, 500, 750, and 1000 nm) based on the Rayleigh and simplified Mie scattering models. Figure 4 shows the directional distribution of the scattering intensity for both T_{15} and T_{250} at different wavelengths. Figure 4a–d show the angular scattering intensity distributions of the T_{15} NPs calculated under the Rayleigh scattering approximation[39] (i.e., $I(\theta) = I_0 \cdot (\frac{2\pi}{\lambda})^4 \cdot (\frac{n^2-1}{n^2+2})^2 \cdot \frac{V^2}{R^2} \cdot (1 + \cos^2\theta)$ where $I(\theta)$ is the scattered light intensity, I_0 is the incident light intensity, λ is the wavelength of the incident light, n is the refractive index of the scattering particle (for TiO_2, n = ~2.5), V is the volume of the particle, R is the distance to the observation point, and θ is the scattering angle). At all wavelengths, the normalized scattering intensity distributions exhibited a characteristic bimodal angular distribution pattern, with maxima at 0° and 180° and a minimum at 90°, consistent with classical Rayleigh scattering behavior. This indicates that both forward and backward scattering are prominent at particle sizes considerably smaller than the incident wavelength, whereas side scattering is relatively weak. Although the shapes of the curves were similar across wavelengths, the overall scattering intensity decreased with an increase in the wavelength. Figure 4e–h show the angular distributions for the T_{250} based on a simplified Mie scattering approximation[40] (i.e., $I(\theta) = (1 + \cos^2\theta) \cdot \exp[-2(1 - \cos\theta) \cdot x$, where x is the size parameter (= $2\pi r/\lambda$), and r is the particle radius); the normalized intensity profiles are also presented for each wavelength (λ = 250, 500, 750, and 1000 nm). At λ = 250 nm, the scattering was strongly forward-directed with a sharp peak at 0° and negligible intensity in the backward direction, which is characteristic of Mie-type scattering. The angular distribution turned broader and more symmetric with an increase in the wavelength, and at λ = 1000 nm, the intensities at 0° and 180° become nearly equal—approaching a Rayleigh-like distribution. This trend reflects a transition from Mie to Rayleigh scattering behavior as the relative size of the particle with respect to the wavelength decreases.

The distributions of T_{15} and T_{250} NPs in the ETL were investigated via FE-SEM and HRLV-SEM analyses, and the results are presented in Figure 5. As shown in Figure 5a,b, in the case of sample S1, wherein only pure T_{15} NPs were used, a highly uniform ETL TF was successfully formed. However, as the T_{250} NP content increased (in samples S2 through S5), aggregation of large particles, such as T_{250}, was observed during the spin-coating process; these particles formed clusters both within and on the surface of the T_{15} matrix-based TF. The particle clustering, surface roughness, and interparticle spacing increased with an increase in the T_{250} content. Notably, in S5, which consisted of T_{250} NPs alone (and no T_{15} NPs), the ETL TF exhibited relatively large gaps and significantly lower TiO_2 packing density. This morphology is expected to maximize light scattering in the absence of T_{15} NPs. However, such voids between TiO_2 NPs may serve as recombination sites for charge carriers when applied as a photoactive layer in solar cells, potentially leading to decreased device performance. Figure 5c shows a cross-sectional HRLV-SEM image of the FTO/c-TiO_2/m-TiO_2/$MAPbI_3$/Spiro-OMeTAD TF, in which the perovskite $MAPbI_3$ and HTL Spiro-OMeTAD were deposited onto ETLs with T_{15} and T_{250} NPs mixed in various ratios. With an increase in the amount of T_{250} in the T_{15} matrix, the average thickness of the FTO/c-TiO_2/m-TiO_2/$MAPbI_3$/Spiro-OMeTAD TFs increased: 591 nm (S1), 1182 nm (S2), 1273 nm (S3), 1364 nm (S4), and 1546 nm (S5).

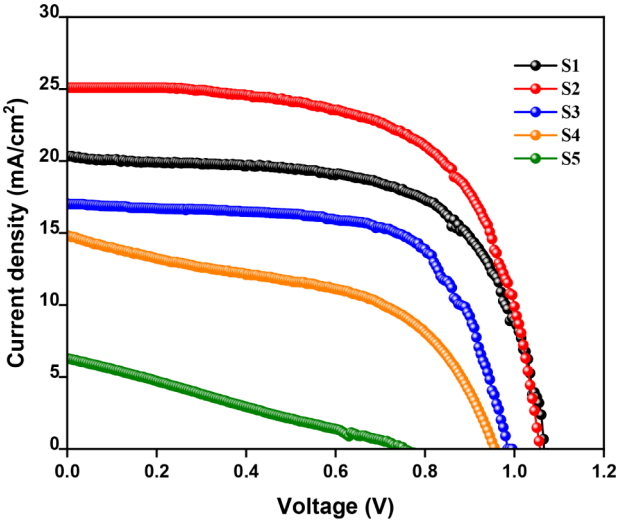

Figure 6. Current density–voltage (J–V) curves of perovskite solar cells (PSCs) fabricated with electron transport layer (ETL) thin films (TFs) composed of various T_{15}:T_{250} mixing ratios: S1 (10:0), S2 (7:3), S3 (5:5), S4 (3:7), and S5 (0:10).

Figure 6 and Table 2 show the current density–voltage (J–V) characteristics of the PSCs fabricated with the ETL TFs with various T_{15}:T_{250} ratios. The measurements were conducted under standard AM 1.5G and 1 sun (1000 W/m^2 illumination conditions. Sample S2 (T_{15}:T_{250} = 7:3) exhibited the highest J_{sc}, V_{oc}, and FF, and thus, the best PCE. This superior performance is attributed to the porous structure of T_{15}, which facilitates uniform infiltration of the perovskite precursor solution and promotes effective electron transport. Moreover, the inclusion of T_{250} NPs enhances light scattering, thereby improving light absorption. In particular, the size of T_{250} NPs, which is comparable to the wavelength of sunlight, ensures efficient Mie scattering, increasing optical path length within the device and maximizing light absorption. In contrast, Rayleigh scattering, which originates from much smaller particles, is dominant at shorter wavelengths; accordingly, its contribution to absorption in the longer wavelength range is minimal. Therefore, the appropriate incorporation of T_{250} NPs into the T_{15} NP matrix can induce effective light harvesting across the entire solar spectrum. In contrast, samples S3 (T_{15}:T_{250} = 5:5) to S5 (T_{15}:T_{250} = 0:10) exhibited a gradual decrease in current density and voltage, possibly attributed to the excess T_{250} content, which may hinder electron transport or interfacial contact and potentially disrupt the uniform formation of the perovskite film, ultimately reducing charge collection efficiency. Hence, the optimal combination of T_{15} and T_{250} in the ETL TF plays a critical role in balancing light absorption mechanisms, charge transport, and interface optimization, thereby enabling high-performance PSC operation.

Figure 7 shows the IPCE spectra of the PSCs incorporating ETL TFs with various mixing ratios of T_{15} and T_{250}, measured

https://doi.org/10.1021/acsaem.5c02634
ACS Appl. Energy Mater. 2025, 8, 14893–14901

Table 2. Photovoltaic Parameters of Perovskite Solar Cells (PSCs) as a Function of Different T_{15}:T_{250} Mixing Ratios in the Electron Transport Layer (ETL) Thin Films (TFs): S1 (10:0), S2 (7:3), S3 (5:5), S4 (3:7), and S5 (0:10)

Samples	J_{SC} (mA/cm^2)	V_{OC}(V)	FF	PCE (%)
S1	20.24 ± 0.53	1.08 ± 0.01	0.620 ± 0.034	13.62 ± 0.28
S2	25.04 ± 0.06	1.06 ± 0.01	0.633 ± 0.001	16.90 ± 0.01
S3	15.95 ± 1.14	0.93 ± 0.07	0.631 ± 0.039	9.45 ± 1.95
S4	14.27 ± 1.09	0.98 ± 0.01	0.536 ± 0.013	7.55 ± 0.87
S5	5.90 ± 0.27	0.80 ± 0.10	0.288 ± 0.017	1.38 ± 0.20

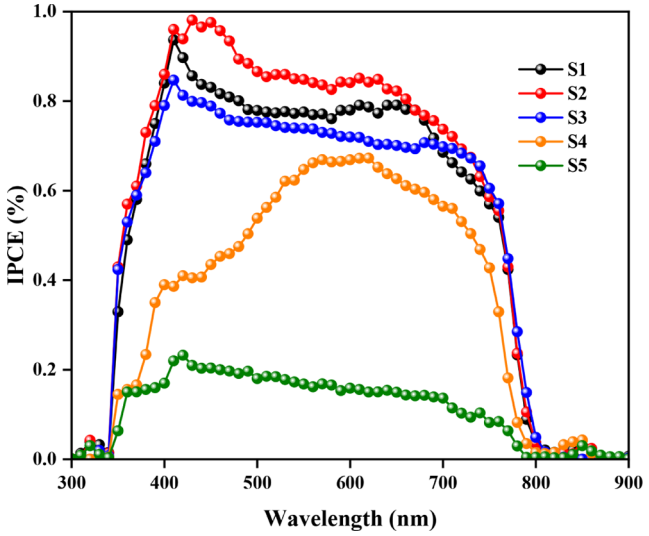

Figure 7. IPCE spectra of fabricated perovskite solar cells (PSCs) with electron transport layer (ETL) thin films (TFs) composed of different T_{15}:T_{250} mixing ratios: S1 (10:0), S2 (7:3), S3 (5:5), S4 (3:7), and S5 (0:10).

in the wavelength range of 300−900 nm. The J_{sc} measured from IPCE spectra for S1, S2, S3, S4 and S5 were 19.5, 22.5, 18.3, 11.0, and 4.3 mA/cm,^{2} respectively. The J_{sc} values measured from IPCE spectra were marginally lower than the J_{sc} values obtained from the J−V curves. This is quite possibly the IPCE spectra were measured under the monochromatic condition without applying white light bias, yielded for lower carrier density and filling of trap state than J_{sc} measured from J-V curve under 1 sun illumination condition. Sample S2 exhibited the highest IPCE values across the entire wavelength range, maintaining values close to 0.9 in the 350−800 nm region, indicating that the 7:3 mixing ratio of T_{15}:T_{250} is the most favorable condition for light absorption and charge generation. Although the IPCE of S1 (10:0) was marginally lower than that of S2 (7:3), it maintained relatively stable performance. The IPCE of S3 (5:5) was moderately lower than that of S1. In contrast, S4 (3:7) and S5 (0:10) demonstrated a sharp drop in IPCE. In particular, S5, composed solely of T_{250}, exhibited very low IPCE across all wavelengths, indicating inefficient light absorption and photocurrent generation. This trend can be interpreted as follows. The porous structure of T_{15} facilitates effective infiltration of the perovskite precursor and contributes to uniform interface formation, while an appropriate amount of T_{250} induces Mie scattering, which extends the optical path length and enhances light harvesting. However, at excess T_{250} content, although the scattering effect continues to play a role, structural degradation of the ETL, interfacial inhomogeneity, and incomplete formation of the PL likely lead to a significant decrease in the overall device efficiency. These observations are in good agreement with the J−V characteristics (Figure 6) and optical properties (Figure 3), reinforcing the conclusion that an optimized combination of T_{15} and T_{250} in the ETL is a critical factor for achieving high-performance PSCs.

4. CONCLUSIONS

In this study, we fabricated PSCs by introducing an ETL TF comprising a mixture of small TiO_2 (T_{15}) NPs and relatively larger TiO_2 (T_{250}) NPs. We systematically examined the effects of the electron transport characteristics accorded by T_{15} and the light scattering effect induced by T_{250} within the ETL TF on the photovoltaic performance of the PSCs. T_{15} NPs, with an average size of several tens of nanometers, form a mesoporous structure that facilitates uniform infiltration of the perovskite solution and provides favorable pathways for electron transport. In contrast, the T_{250} NPs, with sizes measuring several hundred nanometers and comparable to the wavelength of the incident light, induce Mie scattering, which extends the optical path length and significantly enhances light harvesting. In addition, Rayleigh scattering, which typically occurs with particles much smaller than the wavelength of light (e.g., smaller than T_{15}), causes strong scattering primarily at shorter wavelengths and has a limited effect on light absorption in the longer wavelength range. The diffuse reflectance and IPCE spectra measurements indicated that sample S2 (T_{15}:T_{250} = 7:3) exhibited an IPCE response approaching 0.9 in the 350−800 nm range, outperforming sample S1 (T_{15}:T_{250} = 10:0), demonstrated improved light harvesting across a broader wavelength range. The J_{sc}, derived from the J−V curves, was 21.06 mA/cm^2 for S1 and 25.09 mA/cm^2 for S2. The corresponding PCEs were 13.62 and 16.90%, respectively, indicating an approximate 24% improvement in device performance. These results confirm that the light scattering effect of T_{250} effectively enhances light absorption and charge carrier generation. However, in samples with high T_{250} content—S3 (5:5), S4 (3:7), and S5 (0:10)—all photovoltaic parameters, including J_{sc}, V_{oc}, FF, and IPCE, decreased significantly, suggesting that an overabundance of T_{250} may induce unwanted backscattering, hinder the infiltration and formation of the perovskite layer, and increase charge recombination, ultimately degrading the overall device performance. In conclusion, an appropriate mixing ratio of T_{15} and T_{250} is crucial to balancing the optical and electronic properties within the ETL, and incorporating T_{250} at optimal amounts, which can effectively induce Mie scattering, is a promising strategy for achieving high-efficiency PSCs.

AUTHOR INFORMATION

Corresponding Author

Soo Hyung Kim − *Department of Nano Fusion Technology, College of Nanoscience and Nanotechnology and Research Center of Energy Convergence Technology, Pusan National University, Busan 46241, Republic of Korea; Department of*

https://doi.org/10.1021/acsaem.5c02634
ACS Appl. Energy Mater. 2025, 8, 14893−14901

Nanoenergy Engineering, College of Nanoscience and Nanotechnology, Pusan National University, Busan 46241, Republic of Korea; orcid.org/0000-0003-1429-2369; Email: sookim@pusan.ac.kr

Authors

Raji Radhakrishnan − *Department of Nano Fusion Technology, College of Nanoscience and Nanotechnology, Pusan National University, Busan 46241, Republic of Korea*

Jung Keun Cha − *Research Center of Energy Convergence Technology, Pusan National University, Busan 46241, Republic of Korea*

Complete contact information is available at: https://pubs.acs.org/10.1021/acsaem.5c02634

Notes

The authors declare no competing financial interest.

■ ACKNOWLEDGMENTS

This research was supported by grants from the National Research Foundation of the Republic of Korea, funded by the Ministry of Education (grant no. 2020R111A3061095). This study was partly supported by the Korea Institute of Energy Technology Evaluation and Planning (KETEP) funded by the Korea government (MOTIE) (grant no. 20214000000140) through the Graduate School of Convergence for Clean Energy Integrated Power Generation.

■ REFERENCES

(1) Cheng, P.; Zhan, X. Stability of organic solar cells: Challenges and strategies. *Chem. Soc. Rev.* **2016**, *45* (9), 2544−2582.
(2) Tong, Y.; Xiao, Z.; Du, X.; Zuo, C.; Li, Y.; Lv, M.; Yuan, Y.; Yi, C.; Hao, F.; Hua, Y.; et al. Progress of the key materials for organic solar cells. *Sci. China: Chem.* **2020**, *63* (6), 758−765.
(3) Fan, X.; Zhang, M.; Wang, X.; Yang, F.; Meng, X. Recent progress in organic−inorganic hybrid solar cells. *J. Mater. Chem. A* **2013**, *1* (31), 8694−8709.
(4) He, R.; Ren, S.; Chen, C.; Yi, Z.; Luo, Y.; Lai, H.; Wang, W.; Zeng, G.; Hao, X.; Wang, Y.; Zhang, J.; Wang, C.; Wu, L.; Fu, F.; Zhao, D. Wide-bandgap organic−inorganic hybrid and all-inorganic perovskite solar cells and their application in all-perovskite tandem solar cells. *Energy Environ. Sci.* **2021**, *14* (11), 5723−5759.
(5) Choi, H.; Ryu, S. U.; Lee, D. H.; Kim, H.; Song, S.; Kim, H. I.; Park, T. Advancements in organic-based hybrid tandem solar cells: Considering light absorption and spectral matching of organic materials. *ACS Energy Lett.* **2024**, *9*, 3136−3168.
(6) Seok, S. I.; Grätzel, M.; Park, N. G. Methodologies toward highly efficient perovskite solar cells. *Small* **2018**, *14* (20), 1704177.
(7) Chen, B.; Song, J.; Dai, X.; Liu, Y.; Rudd, P. N.; Hong, X.; Huang, J. Synergistic effect of elevated device temperature and excess charge carriers on the rapid light-induced degradation of perovskite solar cells. *Adv. Mater.* **2019**, *31* (35), 1902413.
(8) Zang, L.; Zhao, C.; Hu, X.; Tao, J.; Chen, S.; Chu, J. Emerging trends in electron transport layer development for stable and efficient perovskite solar cells. *Small* **2024**, *20* (26), 2400807.
(9) Faghihnasiri, M.; Izadifard, M.; Ghazi, M. E. Study of strain effects on electronic and optical properties of $CH_3NH_3PbX_3$ (X = Cl, Br, I) perovskites. *Phys. B Condens. Matter.* **2020**, *582*, 412024.
(10) Sani, F.; Shafie, S.; Lim, H. N.; Musa, A. O. Advancement on lead-free organic-inorganic halide perovskite solar cells: A review. *Materials* **2018**, *11* (6), 1008.
(11) Li, T.; Pan, Y.; Wang, Z.; Xia, Y.; Chen, Y.; Huang, W. Additive engineering for highly efficient organic−inorganic halide perovskite solar cells: Recent advances and perspectives. *J. Mater. Chem. A* **2017**, *5* (25), 12602−12652.
(12) Chen, H.; Liu, G.; Ke, L.; Liu, G.; Zhou, C.; Li, H. Alleviating the angular dependence of perovskite solar cells via light-harvesting nanostructure. *Sol. RRL.* **2024**, *8* (12), 2400214.
(13) Ioakeimidis, A.; Papadas, I. T.; Koutsouroubi, E. D.; Armatas, G. S.; Choulis, S. A. Thermal analysis of metal-organic precursors for functional Cu: NiO_x hole transporting layer in inverted perovskite solar cells: Role of solution combustion chemistry in Cu: NiO_x thin films processing. *Nanomaterials* **2021**, *11* (11), 3074.
(14) Kim, M.; Alfano, A.; Perotto, G.; Serri, M.; Dengo, N.; Mezzetti, A.; Gross, S.; Prato, M.; Salerno, M.; Rizzo, A.; Sorrentino, R.; Cescon, E.; Meneghesso, G.; Fonzo, F. D.; Petrozza, A.; Gatti, T.; Lamberti, F. Moisture resistance in perovskite solar cells attributed to a water-splitting layer. *Commun. Mater.* **2021**, *2* (1), 6.
(15) Li, S.; Cao, Y.-L.; Li, W.-H.; Bo, Z.-S. A brief review of hole transporting materials commonly used in perovskite solar cells. *Rare Met.* **2021**, *40*, 2712−2729.
(16) Ulfa, M.; Zhu, T.; Goubard, F.; Pauporté, T. Molecular versus polymeric hole transporting materials for perovskite solar cell application. *J. Mater. Chem. A* **2018**, *6* (27), 13350−13358.
(17) Calió, L.; Kazim, S.; Grätzel, M.; Ahmad, S. Hole-transport materials for perovskite solar cells. *Angew. Chem., Int. Ed.* **2016**, *55* (47), 14522−14545.
(18) Saliba, M.; Matsui, T.; Domanski, K.; Seo, J. Y.; Ummadisingu, A.; Zakeeruddin, S. M.; Correa-Baena, J. P.; Tress, W. R.; Abate, A.; Hagfeldt, A. Incorporation of rubidium cations into perovskite solar cells improves photovoltaic performance. *Science* **2016**, *354*, 206−209.
(19) Wang, M.; Cao, F.; Deng, K.; Li, L. Adduct phases induced controlled crystallization for mixed-cation perovskite solar cells with efficiency over 21%. *Nano Energy* **2019**, *63*, 103867.
(20) Ma, S.; Pang, S.; Dong, H.; Xie, X.; Liu, G.; Dong, P.; Liu, D.; Zhu, W.; Xi, H.; Chen, D.; Zhang, C.; Hao, Y. Stability improvement of perovskite solar cells by the moisture-resistant PMMA: Spiro-OMeTAD hole transport layer. *Polymers* **2022**, *14*, 343.
(21) Mali, S. S.; Hong, C. K. p-i-n/n-i-p type planar hybrid structure of highly efficient perovskite solar cells towards improved air stability: Synthetic strategies and the role of p-type hole transport layer (HTL) and n-type electron transport layer (ETL) metal oxides. *Nanoscale* **2016**, *8*, 10528−10540.
(22) Sarkar, A.; Jeon, N. J.; Noh, J. H.; Seok, S. I. Well-organized mesoporous TiO_2 photoelectrodes by block copolymer-induced sol-gel assembly for inorganic-organic hybrid perovskite solar cells. *J. Phys. Chem. C* **2014**, *118* (30), 16688−16693.
(23) Khaleel, O. A.; Ahmed, D. S. Interface engineering at electron transport/perovskite layers using wetting mesoporous titanium dioxide to fabricate efficient and stable perovskite solar cells. *Int. J. Energy Res.* **2022**, *46* (8), 11163−11173.
(24) Huang, W.; Zhang, R.; Xia, X.; Steichen, P.; Liu, N.; Yang, J.; Chu, L.; Li, X. Room temperature processed double electron transport layers for efficient perovskite solar cells. *Nanomaterials* **2021**, *11* (2), 329.
(25) Mahmood, K.; Sarwar, S.; Mehran, M. T. Current status of electron transport layers in perovskite solar cells: Materials and properties. *RSC Adv.* **2017**, *7* (28), 17044−17062.
(26) Wang, D.; Ye, T.; Zhang, Y. Recent advances of non-fullerene organic electron transport materials in perovskite solar cells. *J. Mater. Chem. A* **2020**, *8* (40), 20819−20848.
(27) Song, Z. H.; Tong, G. Q.; Li, H.; Li, G. P.; Ma, S.; Yu, S. M.; Liu, Q.; Jiang, Y. Three-dimensional architecture hybrid perovskite solar cells using CdS nanorod arrays as an electron transport layer. *Nanotechnology* **2018**, *29*, 025401.
(28) Tong, G.; Song, Z.; Li, C.; Zhao, Y.; Yu, L.; Xu, J.; Jiang, Y.; Sheng, Y.; Shi, Y.; Chen, K. Cadmium-doped flexible perovskite solar cells with a low-cost and low-temperature-processed CdS electron transport layer. *RSC Adv.* **2017**, *7*, 19457−19463.
(29) Sun, X.; Xu, J.; Xiao, L.; Chen, J.; Zhang, B.; Yao, J.; Dai, S. Influence of the porosity of the TiO_2 film on the performance of the perovskite solar cell. *Int. J. Photoenergy* **2017**, *2017*, 4935265.
(30) Zukalová, M.; Zukal, A.; Kavan, L.; Nazeeruddin, M. K.; Liska, P.; Grätzel, M. Organized mesoporous TiO_2 films exhibiting greatly

enhanced performance in dye-sensitized solar cells. *Nano Lett.* **2005**, *5*, 1789−1792.
(31) Brundha, C.; Cha, J. K.; Ren, Q. F.; Kim, H. S.; Lee, H. W.; Kim, S. H. Tuning the pore structures in TiO_2 thin films by polymer templates for high-performance perovskite solar cells. *ACS Appl. Energy Mater.* **2023**, *6* (21), 11081−11089.
(32) Lian, Q.; Mokhtar, M. Z.; Lu, D.; Zhu, M.; Jacobs, J.; Foster, A. B.; Thomas, A. G.; Spencer, B. F.; Wu, S.; Liu, C.; Hodson, N. W.; Smith, B.; Alkaltham, A.; Alkhudhari, O. M.; Watson, T.; Saunders, B. R. Using soft polymer template engineering of mesoporous TiO_2 scaffolds to increase perovskite grain size and solar cell efficiency. *ACS Appl. Mater. Interfaces* **2020**, *12* (16), 18578−18589.
(33) Drygała, A.; Starowicz, Z.; Gawlińska-Nęcek, K.; Karolus, M.; Lipiński, M.; Jarka, P.; Matysiak, W.; Tillová, E.; Palček, P.; Tański, T. Hybrid mesoporous TiO_2/ZnO electron transport layer for efficient perovskite solar cell. *Molecules* **2023**, *28*, 5656.
(34) Yang, H. Y.; Rho, W. Y.; Lee, S. K.; Kim, S. H.; Hahn, Y. B. TiO_2 nanoparticles/nanotubes for efficient light harvesting in perovskite solar cells. *Nanomaterials* **2019**, *9* (3), 326.
(35) Lin, S. H.; Su, Y. H.; Cho, H. W.; Kung, P. Y.; Liao, W. P.; Wu, J. J. Nanophotonic perovskite solar cell architecture with a three-dimensional TiO_2 nanodendrite scaffold for light trapping and electron collection. *J. Mater. Chem. A* **2016**, *4* (3), 1119−1125.
(36) Kim, K. P.; Kim, W. H.; Kwon, S. M.; Kim, J. Y.; Do, Y. S.; Woo, S. Enhanced light absorption by facile patterning of nano-grating on mesoporous TiO_2 photoelectrode for cesium lead halide perovskite solar cells. *Nanomaterials* **2021**, *11* (5), 1233.
(37) Li, N.; Yan, J.; Ai, Y.; Jiang, E.; Lin, L.; Shou, C.; Yan, B.; Sheng, J. A low-temperature TiO_2/SnO_2 electron transport layer for high-performance planar perovskite solar cells. *Sci. China Mater.* **2020**, *63*, 207−215.
(38) Wu, J.; Wang, Y.; Su, C.; Zhou, H.; Xu, H.; Jin, L. Preparation and characterization of planar heterojunction perovskite solar cells based on c-TiO_2/$CH_3NH_3PbI_3$/HTM/Ag structure. *J. Sol-Gel Sci. Technol.* **2021**, *100*, 440.
(39) Seinfeld, J. H.; Pandis, S. N. *Atmospheric Chemistry and Physics*, 2nd ed.; John Wiley and Sons: NJ, 2006.
(40) Gordon, J. E. Simple method for approximating Mie scattering. *J. Opt. Soc. Am. A* **1985**, *2*, 156−159.

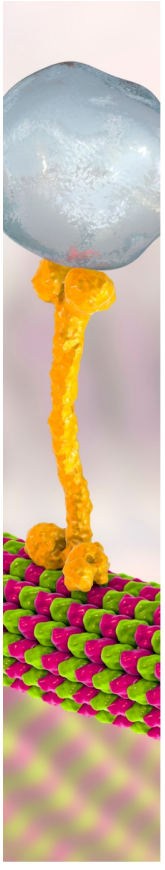
CAS BIOFINDER DISCOVERY PLATFORM™
BRIDGE BIOLOGY AND CHEMISTRY FOR FASTER ANSWERS
Analyze target relationships, compound effects, and disease pathways
Explore the platform
CAS
A division of the American Chemical Society

https://doi.org/10.1021/acsaem.5c02634
ACS Appl. Energy Mater. 2025, 8, 14893−14901